Ultrathin-enhanced ferroelectricity directly on silicon

Suraj S. Cheema,[1*] Daewoong Kwon,[2*] Nirmaan Shanker,[1,2] Roberto dos Reis,[3] Shang-Lin Hsu,[3] Jun Xiao,[4] Haigang Zhang,[5] Ryan Wagner,[5] Adhiraj Datar,[1,2] Margaret R. McCarter,[6] Claudy R. Serrao,[2] Ajay K. Yadav,[2] Golnaz Karbasian,[2] Cheng-Hsiang Hsu,[2] Ava Tan,[2] Li-Chen Wang,[1] Vishal Thakare,[1] Xiang Zhang,[4,7] Apurva Mehta,[8] Evguenia Karapetrova,[9] Rajesh Chopdekar,[10] Padraic Shafer,[10] Elke Arenholz,[10,11] Chenming Hu,[2] Roger Proksch,[5] Ramamoorthy Ramesh,[1,6] James Ciston,[3] Sayeef Salahuddin[2,7]

[1] *Department of Materials Science and Engineering, University of California, Berkeley, California 94720, USA*

[2] *Department of Electrical Engineering and Computer Sciences, University of California, Berkeley, California 94720, USA*

[3] *National Center for Electron Microscopy, Molecular Foundry, Lawrence Berkeley National Laboratory, Berkeley, California 94720, USA*

[4] *NSF Nanoscale Science and Engineering Center, University of California, Berkeley, California 94720, USA*

[5] *Asylum Research, an Oxford Instruments Company, Santa Barbara, California 93117, USA*

[6] *Department of Physics, University of California, Berkeley, Berkeley, California 94720, USA*

[7] *Materials Sciences Division, Lawrence Berkeley National Laboratory, Berkeley, California 94720, USA*

[8] *Stanford Synchrotron Radiation Lightsource, SLAC National Accelerator Laboratory, Menlo Park, California 94025, USA*

[9] *Advanced Photon Source, Argonne National Laboratory, Argonne, Illinois 60439, USA*

[10] *Advanced Light Source, Lawrence Berkeley National Laboratory, Berkeley, California 94720, USA*

[11] *Cornell High Energy Synchrotron Source, Cornell University, Ithaca, New York 14853, USA*

**These authors contributed equally to this work*

The critical size limit of electric polarization remains a fundamental question in nanoscale ferroelectric research[1]. As such, the viability of ultrathin ferroelectricity greatly impacts emerging low-power logic and nonvolatile memories[2]. Size effects in ferroelectrics have been thoroughly investigated for perovskite oxides – the archetypal ferroelectric system[3]. Perovskites, however, have so far proved unsuitable for thickness-scaling and integration with modern semiconductor processes[4]. Here, we report ultrathin ferroelectricity in doped-HfO_2, a fluorite-structure oxide grown by atomic layer deposition on silicon. We demonstrate the persistence of inversion symmetry breaking and spontaneous, switchable polarization down to 1 nm. Our results indicate not only the absence of a ferroelectric critical thickness, but also enhanced polar distortions as film thickness is reduced, contradictory to perovskite ferroelectrics. This work shifts the focus on the fundamental limits of ferroelectricity to simpler transition metal oxide systems – from perovskite-derived complex oxides to fluorite-structure binary oxides – in which 'reverse' size effects counter-intuitively stabilize polar symmetry in the ultrathin regime.

Ferroelectric materials exhibit stable states of collectively ordered electrical dipoles whose polarization can be reversed under an applied electric field[5]. Consequently, ultrathin ferroelectrics are of great technological interest for high-density electronics, particularly field-effect transistors and nonvolatile memories[2]. However, ferroelectricity is typically suppressed at the few nanometer scale in the ubiquitous perovskite oxides[6]. First-principles calculations predict six unit cells as the critical thickness in perovskite ferroelectrics[1] due to incomplete screening of depolarization fields[3]. Atomic-scale ferroelectricity in perovskites often fail to demonstrate polarization switching[7,8], a crucial ingredient for application. Furthermore, attempts to synthesize ferroelectric perovskite films on silicon[9,10] are plagued by chemical incompatibility[4,11] and high temperatures required for epitaxial growth. Since the discovery of ferroelectricity in HfO_2-based thin films in 2011[12], fluorite-structure binary oxides (fluorites) have attracted considerable interest[13] as they enable low-temperature synthesis and conformal growth in three-dimensional (3D) structures on silicon[14,15], thereby overcoming many of the issues that restrict its perovskite counterparts in terms of complementary metal-oxide-semiconductor (CMOS) compatibility and thickness scaling[16]. Considering the extensive implications for future computing[2,17,18], achieving ferroelectricity in sub-

2 nm doped-HfO_2 is highly desirable for realizing ultra-scaled CMOS-compatible ferroelectric-based devices beyond the 5 nm technology node[19].

Here we demonstrate ultrathin ferroelectricity down to 1 nm $Hf_{0.8}Zr_{0.2}O_2$ (HZO), grown by low-temperature atomic layer deposition (ALD) on silicon. Second harmonic generation and advanced scanning probe techniques establish the presence of inversion symmetry breaking and switchable electric polarization, respectively. Not only is ferroelectricity stabilized in ultrathin HZO, but spectroscopic and diffraction signatures of its fluorite-structure symmetry also indicate enhanced polar distortion in the ultrathin regime. Such size effects in this fluorite-structure system are contrary to its perovskite counterparts[6], which can be understood from symmetry considerations. In classical perovskites, surface-energy-driven size effects at reduced dimensions favor the high-symmetry paraelectric phase (cubic) over the low-symmetry ferroelectric phase (tetragonal)[20]. Conversely in fluorites, the noncentrosymmetric phase (orthorhombic $Pca2_1$, O-phase) is higher-symmetry relative to the bulk-stable centrosymmetric phase ($P2_1/c$, M-phase)[21]. Consequently, surface energies can promote (destabilize) inversion symmetry breaking in fluorite (perovskite) ferroelectrics in the 2D limit[21,22]. Due to this size-induced noncentrosymmetry – i.e. 'reverse' size effects (Fig. 1a, Extended Data Fig. 1) – HZO present a promising model system to explore the ultrathin limits of ferroelectricity.

Thin films of HZO are grown using ALD down to 10 cycles on oxidized silicon at 250°C. For reference, approximately 11 ALD cycles correspond to 1 nm thickness, as confirmed by x-ray reflectivity (XRR, Extended Data Fig. 2) and transmission electron microscopy (TEM, Extended Data Fig. 3). Subsequently, HZO films are capped by a metal and subjected to rapid thermal annealing (RTA) – henceforth referred to as confinement strain (Fig. 1c) – to impart anisotropic thermal stresses. Confinement strain has been reported to help distort the high-symmetry tetragonal fluorite-structure polymorph ($P4_2/nmc$, T-phase) into the polar O-phase[13] (Fig. 1a). For confined ultrathin HZO films, x-ray diffraction analysis indicates a highly-oriented noncentrosymmetric structure in contrast to polycrystalline thicker films (Extended Data Fig. 4). Inversion symmetry breaking in 10 cycle (~ 1 nm) HZO films is confirmed by the presence of second harmonic generation (SHG) (Extended Data Fig. 5), previously employed to demonstrate two-dimensional ferroelectricity in an atomically thin layered system[23].

Beyond inversion asymmetry, ferroelectricity also requires electrical switching between polarization states. Resonance-enhanced piezoresponse force microscopy (PFM) demonstrates bistable switching in $Si/SiO_2/HZO$ heterostructures (Fig. 2a). PFM phase images on 10 cycle HZO films (Fig. 2d) show well-defined regions of opposite 180° phase contrast – corresponding to remnant polarization states (Fig. 2b) – that can be rewritten in a nonvolatile fashion. Notably, unpoled regions demonstrate the same phase contrast as positively poled regions (Fig. 2d), indicating ultrathin HZO exhibits spontaneous polarization. In previous studies, field cycling is often required to 'wake-up' the ferroelectricity in HfO_2-based fluorites, attributed to a field-induced nonpolar-polar phase transition[13]. Here, atomic-scale thickness in tandem with mechanical confinement enhances the polar phase stability to exhibit spontaneous polarization, eliminating one of the most critical issue plaguing fluorite-structure ferroelectrics[16]. RTA alone is insufficient for ferroelectricity; regions of HZO annealed without a metal capping layer do not exhibit ferroelectric signatures (Extended Data Fig. 6). This highlights the critical role of ultrathin confinement – and the strains imposed by such layering – on stabilizing the polar O-phase in ultrathin fluorite-structure films.

Along with phase contrast imaging, local PFM switching spectroscopy further confirm the robust ferroelectricity in 10 cycle HZO films, as demonstrated by 180° phase hysteresis and butterfly-shape amplitude (d_{33}) loops (Fig. 2e). PFM spectroscopy was performed on metal electrodes to eliminate electrostatic artifacts from the tip[24] and potential electromechanical contributions (Methods). In addition, careful monitoring of topography has been performed during poling (Extended Data Fig. 7a) to detect the possibility of any electrochemical and electromechanical artifacts. Time-dependent PFM imaging (Extended Data Fig. 7b) on 10 cycle HZO illustrates polarization patterns sustain for at least 24 hours; such long-term retention suggests PFM contrast is due to ferroelectric behavior and not shorter-scale spurious contributions often attributed to amorphous hafnia[25]. Furthermore, V_{ac}-dependent piezoresponse loops (Extended Data Fig. 7c) rule out electrostatic artifacts from charging[25]. Moving beyond the standard PFM optical beam detection method, interferometric displacement sensor (IDS) PFM measurements (Extended Data Fig. 7d) definitively demonstrate the ferroelectric origin of switching spectroscopy hysteresis in 10 cycle HZO. The recently developed IDS technique[26] eliminates long-range electrostatics and cantilever resonance artifacts which obfuscate typical voltage-modulated PFM. Contact IDS measurements demonstrate 180° phase hysteresis and butterfly-shape d_{33}, indicative of

ferroelectric behavior free of electrostatic contributions[26]. A lack of electrostatically driven hysteresis is confirmed by off-surface measurements (Extended Data Fig. 7d). Along with IDS, scanning capacitance microscopy (SCM) provides another advanced scanning probe technique to conclusively probe ferroelectricity in ultrathin HZO. SCM differential capacitance spectroscopy on 10 cycle HZO demonstrates butterfly-shape capacitance-voltage (*C*-*V*) hysteresis (Fig. 2c, Extended Data Fig. 8). The microwave-frequency detection in SCM (Methods) mitigates leakage currents which prevent typical bulk electrical characterization of ultrathin ferroelectrics, and provides definitive evidence of ferroelectric polarization switching beyond PFM spectroscopy

To examine the structural and electronic origins of ferroelectricity in HZO, we employ grazing-incidence x-ray diffraction (GI-XRD) and x-ray absorption spectroscopy (XAS) (Fig. 3). GI-XRD alone cannot unambiguously distinguish between certain fluorite-structure polymorphs in ultrathin HZO; as a complement to diffraction, XAS provides spectroscopic signatures of the polar O-phase and nonpolar T-phase. In particular, the T-phase nonpolar distortion (D_{4h}, 4-fold prismatic symmetry) from regular tetrahedral to fluorite-structure symmetry does not split the degenerate *e*-bands (d_{x2-y2}, d_{3z2-r2}). Meanwhile, the O-phase polar rhombic pyramidal distortion (C_{2v}, 2-fold pyramidal symmetry) does split the *e*-manifold, providing a symmetry-specific spectroscopic marker (Extended Data Fig. 9a,b). Due to the d^0 electronic configuration present in Hf^{4+} (Zr^{4+}), spectral weight from oxygen *K*-edge XAS can be attributed solely to crystal field effects, providing additional insights into the degree of structural distortion. The spectral weight of the symmetry-split *e*-regimes (Extended Data Fig. 9c) and pre-edge regime (Extended Data Fig. 9e) increases with decreasing thickness, indicative of more pronounced rhombic distortion and divergence from isotropic nearest-neighbor oxygen polyhedral coordination (Extended Data Fig. 9d), respectively. These spectral weight trends provide further evidence of ultrathin-enhanced distortions. In conjunction with XAS, x-ray linear dichroism (XLD) can also probe structural distortions due to its sensitivity to orbital asymmetry. Nanospectroscopy via soft x-ray photoemission electron microscopy (PEEM) illustrates spatially resolved XLD contrast at 535 eV (Extended Data Fig. 9f), corresponding to the *e*-split rhombic distortion regime. This suggests XLD at the O *K*-edge is indeed sensitive to polar features in ultrathin HZO. Shifting to sample-averaged XLD at the Zr M_2-edge, the orbital polarization is found to increase from the thick (100 cycle) to

ultrathin (10 cycle) regime (Fig. 3c), indicative of increased oxygen polyhedral distortion (Fig. 3d) consistent with ultrathin-enhanced ferroelectricity.

Remarkably, we also observe the emergence of crystallographic texturing of HZO films in the ultrathin regime (Fig. 1b, 3e). Note that many of the reflections in 100 cycles HZO – including the dominant (111) – are absent in the GI-XRD spectra below 25 cycles due to geometric limitations of 1D spectra to detect all reflections present in highly-oriented films (Methods). Tilted-geometry (φ-χ) diffraction i.e. pole figures are required to access these oriented reflections at specific points – rather than polycrystalline-like rings – in reciprocal space. The spot-like patterns present in pole figures about the (111) reflections (Extended Data Fig. 4c) confirm the high-degree of texturing in ultrathin HZO. Interestingly, this texturing happens despite local nanocrystalline regions observed in TEM for ultrathin films (e.g. 15 cycles HZO in Extended Data Fig. 3d). Coinciding with the onset of texturing, the microstructural evolution below 25 cycles HZO manifests spectroscopically as inverted orbital polarization at the *e*-manifold (Fig. 3b), suggesting flipped polar-distortion-split *e*-levels (d_{x2-y2} and d_{3z2-r2}). This indicates that sub-25 cycle ultrathin films enter a new electronic structure concurrently as the crystalline structure orders. Therefore, confinement strain in atomic-scale fluorite films could offer a novel route to tailor electronic structure and engineer polarization at the orbital-level[27] akin to epitaxial strain in perovskite films.

The onset of highly-ordered films also coincides with sharp rises in structural markers of distortion (Fig. 3g). The degree of rhombic distortion is captured by the lattice spacing d_{111}; accordingly, d_{111} is tied to macroscopic polarization in HZO[28,29]. We observe increasing d_{111} with decreasing thickness (Fig. 3g) – as previously reported in epitaxial HZO films grown by pulsed laser deposition (PLD)[28,29] – consistent with ultrathin-enhanced ferroelectricity. Notably, our low-temperature ALD-grown films on silicon can induce similar structurally-induced phenomena observed in high-temperature PLD-grown epitaxial films on perovskite templates and extended to an even thinner limit. Furthermore, the d_{111} bifurcation below 25 cycles suggests a link between texturing and amplified distortion in the ultrathin regime. Another crystallographic signature – orthorhombic aspect ratio ($^{2c}/_{a+b}$) – also indicates enhanced distortions in the ultrathin regime (Fig. 3g). Fluorite-structure orthorhombicity[13] is akin to perovskite tetragonality[30] ($^{c}/_{a}$); these ratios serve as structural barometers of macroscopic polarization. The orthorhombic distortion present in 10 cycle HZO far exceeds any reported values for HfO_2-ZrO_2 polymorphs[13]: we find > 10% aspect

asymmetry, while 3-4% is typically reported for fluorite-structure ferroelectrics, consistent with our thicker films (Fig. 3g). Correspondingly, the tetrahedral and rhombic crystal field splitting energies in ultrathin films surpass expected polar fluorite-structure values by 1.3 eV and 700 meV, respectively (Extended Data Fig. 9g). Such colossal structural splittings are well beyond the reported limits of epitaxial strain in perovskite films[27]. Therefore, although prohibitive tunnel currents prevent accurate quantification of polarization from traditional *P-V* measurements, multiple structural gauges of polarization indicate significant enhancement in the ultrathin limit.

In summary, several techniques self-consistently demonstrate robust ferroelectricity in HZO films down to 1 nm (Extended Data Fig. 2, 3), synthesized by low-temperature ALD on silicon. Remarkably these experiments indicate that polar distortions are amplified in the ultrathin limit; diffraction markers – d_{111} lattice spacing, structural aspect ratio – and spectroscopic signatures – orbital polarization, crystal field splitting – all demonstrate ultrathin enhancement. Such 'reverse' size effects oppose conventional perovskite ferroelectric trends[6]. Previous works on polycrystalline doped-HfO_2[31–33] have explained thickness-dependent polarization trends based on the volume fraction of the ferroelectric O-phase. However, our observations are more consistent with studies of pseudo-epitaxial HZO films grown on perovskite templates[28,29] in that we also observe significant orientation in the ultrathin regime and enhancement of ferroelectricity with decreasing thickness. Importantly, our work demonstrates that this enhancement persists down to at least two fluorite-structure unit cell thickness, overcoming the deleterious depolarization field effects which would otherwise dominate a prototypical perovskite-structure ferroelectric in this ultrathin regime[1,34]. Further studies should explore how the current understanding of film synthesis, phase competition and polar distortion in HZO developed for thicker films (> 5 nm)[35] evolves in the ultrathin regime (< 2 nm). Our results indicate that harnessing confinement strain to amplify atomic displacements in ultrathin films provides a novel route towards enhancing electric polarization at the nanoscale beyond epitaxial strain[36,37], akin to strain gradients in flexoelectricity[38,39]. From a technological perspective, direct monolithic integration of ultrathin doped-HfO_2 on Si/SiO_2 paves the way for polarization-driven low-power resistive memories (Extended Data Fig. 10) and ultra-scaled ferroelectric-based computing[40,41].

REFERENCES

1. Junquera, J. & Ghosez, P. Critical thickness for ferroelectricity in perovskite ultrathin films. *Nature* 422, 506 (2003).
2. Mikolajick, T., Slesazeck, S., Park, M. & Schroeder, U. Ferroelectric hafnium oxide for ferroelectric random-access memories and ferroelectric field-effect transistors. *MRS Bull.* 43, 340–346 (2018).
3. Dawber, M., Rabe, K. M. & Scott, J. F. Physics of thin-film ferroelectric oxides. *Rev. Mod. Phys.* 77, 1083–1130 (2005).
4. Schlom, D. G., Guha, S. & Datta, S. Gate Oxides Beyond SiO_2. *MRS Bull.* 33, 1017–1025 (2008).
5. Lines, M. E. & Glass, A. M. *Principles and applications of ferroelectrics and related materials* (Oxford University Press, 1977).
6. Ahn, C., Rabe, K. & Triscone, J. Ferroelectricity at the Nanoscale: Local Polarization in Oxide Thin Films and Heterostructures. *Science* 303, 488–491 (2004).
7. Fong, D. D. *et al.* Ferroelectricity in Ultrathin Perovskite Films. *Science* 304, 1650–1653 (2004).
8. Tenne, D. A. *et al.* Probing Nanoscale Ferroelectricity by Ultraviolet Raman Spectroscopy. *Science* 313, 1614–1616 (2006).
9. Warusawithana, M. P. *et al.* A Ferroelectric Oxide Made Directly on Silicon. *Science* 324, 367–370 (2009).
10. Dubourdieu, C. *et al.* Switching of ferroelectric polarization in epitaxial $BaTiO_3$ films on silicon without a conducting bottom electrode. *Nat. Nanotechnol.* 8, 748–54 (2013).
11. Schlom, D. G. & Haeni, J. H. A Thermodynamic Approach to Selecting Alternative Gate Dielectrics. *MRS Bull.* 27, 198–204 (2002).
12. Böscke, T. S., Müller, J., Bräuhaus, D., Schröder, U. & Böttger, U. Ferroelectricity in hafnium oxide thin films. *Appl. Phys. Lett.* 99, 102903 (2011).
13. Park, M. H. *et al.* Ferroelectricity and Antiferroelectricity of Doped Thin HfO_2-Based Films. *Adv. Mater.* 27, 1811–1831 (2015).
14. Robertson, J. High dielectric constant gate oxides for metal oxide Si transistors. *Rep. Prog. Phys.* 69, 327 (2006).
15. Muller, J. *et al.* Ferroelectric hafnium oxide: A CMOS-compatible and highly scalable approach to future ferroelectric memories. In *2013 IEEE Int. Electron Devices Meet. (IEDM),* 10.8.1–10.8.4 (IEEE, 2013).
16. Park, M., Lee, Y., Mikolajick, T., Schroeder, U. & Hwang, C. Review and perspective on ferroelectric HfO_2-based thin films for memory applications. *MRS Commun.* 1–14 (2018).
17. Wong, J. C. & Salahuddin, S. Negative Capacitance Transistors. *Proc. IEEE* 107, 49–62 (2019).
18. Kwon, D. *et al.* Improved subthreshold swing and short channel effect in FDSOI n-Channel negative capacitance field effect transistors. *IEEE Electron Device Lett.* 39, 300–303 (2018).
19. Salahuddin, S., Ni, K. & Datta, S. The era of hyper-scaling in electronics. *Nat. Electron.* 1, 442–450 (2018).
20. Merz, W. J. The effect of hydrostatic pressure on the curie point of barium titanate single crystals. *Phys. Rev.* 77 (1950).

21. Ohtaka, O. *et al.* Phase relations and volume changes of hafnia under high pressure and high temperature. *J. Am. Ceram. Soc.* 84, 1369–1373 (2001).
22. Materlik, R., Künneth, C. & Kersch, A. The origin of ferroelectricity in $Hf_{1-x}Zr_xO_2$: A computational investigation and a surface energy model. *J. Appl. Phys.* 117, 134109 (2015).
23. Xiao, J. *et al.* Intrinsic Two-Dimensional Ferroelectricity with Dipole Locking. *Phys. Rev. Lett.* 120, 227601 (2018).
24. Vasudevan, R. K., Balke, N., Maksymovych, P., Jesse, S. & Kalinin, S. V. Ferroelectric or non-ferroelectric: Why so many materials exhibit "ferroelectricity" on the nanoscale. *Appl. Phys. Rev.* 4, 021302 (2017).
25. Balke, N. *et al.* Differentiating ferroelectric and nonferroelectric electromechanical effects with scanning probe microscopy. *ACS Nano* 9, 6484–6492 (2015).
26. Collins, L., Liu, Y., Ovchinnikova, O. S. & Proksch, R. Quantitative Electromechanical Atomic Force Microscopy. *ACS Nano* 13, 8055–8066 (2019).
27. Disa, A. S. *et al.* Orbital engineering in symmetry-breaking polar heterostructures. *Phys. Rev. Lett.* 114 (2015).
28. Wei, Y. *et al.* A rhombohedral ferroelectric phase in epitaxially strained $Hf_{0.5}Zr_{0.5}O_2$ thin films. *Nat. Mater.* 17, 1095–1100 (2018).
29. Lyu, J., Fina, I., Solanas, R., Fontcuberta, J. & Sánchez, F. Growth Window of Ferroelectric Epitaxial $Hf_{0.5}Zr_{0.5}O_2$ Thin Films. *ACS Appl. Electron. Mater.* 1, 220–228 (2019).
30. Schlom, D. G. *et al.* Elastic strain engineering of ferroic oxides. *MRS Bull.* 39, 118–130 (2014).
31. Park, M. H. *et al.* Evolution of phases and ferroelectric properties of thin $Hf_{0.5}Zr_{0.5}O_2$ films according to the thickness and annealing temperature. *Appl. Phys. Lett.* 102, 242905 (2013).
32. Tian, X. *et al.* Evolution of ferroelectric HfO_2 in ultrathin region down to 3 nm. *Appl. Phys. Lett.* 112, 102902 (2018).
33. Richter, C. *et al.* Si Doped Hafnium Oxide - A "Fragile" Ferroelectric System. *Adv. Electron. Mater.* 3, 1700131 (2017).
34. Stengel, M. & Spaldin, N. A. Origin of the dielectric dead layer in nanoscale capacitors. *Nature* 443, 679–82 (2006).
35. Kim, S. J., Mohan, J., Summerfelt, S. R. & Kim, J. Ferroelectric $Hf_{0.5}Zr_{0.5}O_2$ Thin Films: A Review of Recent Advances. *JOM* 71, 246–255 (2019).
36. Schlom, D. G. *et al.* Strain Tuning of Ferroelectric Thin Films. *Annu. Rev. Mater. Res.* 37, 589–626 (2007).
37. Haeni, J. H. *et al.* Room-temperature ferroelectricity in strained $SrTiO_3$. *Nature* 430, 758–61 (2004).
38. Zubko, P., Catalan, G. & Tagantsev, A. K. Flexoelectric Effect in Solids. *Annu. Rev. Mater. Res.* 43, 387–421 (2013).
39. Jariwala, D., Marks, T. J. & Hersam, M. C. Mixed-dimensional van der Waals heterostructures. *Nat. Mater.* 16, 170–181 (2016).
40. Kwon, D. *et al.* Negative Capacitance FET With 1.8-nm-Thick Zr-Doped HfO_2 Oxide. *IEEE Electron Device Lett.* 40, 993–996 (2019).
41. Lee, M. H. *et al.* Physical thickness 1.x nm ferroelectric HfZrOx negative capacitance FETs. In *2016 IEEE Int. Electron Devices Meet. (IEDM)*, 12.1.1–12.1.4 (IEEE, 2016).

Acknowledgements This research was supported in part by the Berkeley Center for Negative Capacitance Transistors (BCNCT), ASCENT, one of six centres in JUMP (Joint University Microelectronics Program), a Semiconductor Research Corporation (S.R.C.) program sponsored by DARPA, and the DARPA T-MUSIC program. This research used resources of the Advanced Photon Source, a U.S. Department of Energy (DOE) Office of Science User Facility operated for the DOE Office of Science by Argonne National Laboratory under Contract No. DE-AC02-06CH11357. This research used resources of the Advanced Light Source, which is a DOE Office of Science User Facility under contract no. DE-AC02-05CH11231. Use of the Stanford Synchrotron Radiation Light source, SLAC National Accelerator Laboratory, is supported by the U.S. Department of Energy, Office of Science, Office of Basic Energy Sciences under Contract No. DE-AC02-76SF00515. Electron microscopy of was performed at the Molecular Foundry, LBNL, supported by the Office of Science, Office of Basic Energy Sciences, US Department of Energy (DE-AC02-05CH11231). J.C. and R.d.R. acknowledge additional support from the Presidential Early Career Award for Scientists and Engineers (PECASE) through the U.S. Department of Energy.

Author Contributions Film synthesis was performed by S.S.C, G.K., and D.K.; electron microscopy was performed by R.d.R. and S.-L.H. under the supervision of J.C. and R.R., respectively and analysis by L.-C.W. under the supervision of S.S.; scanning probe microscopy was performed by S.S.C. and N.S.; interferometric displacement sensor measurements were performed and developed by R.W. and R.P.; scanning capacitance microscopy was performed by H.Z.; x-ray structural characterization was performed by S.S.C., N.S. and M.M. under the supervision of A.M. and E.K.; x-ray spectroscopy was performed by S.S.C under the supervision of R.C., P.S. and E.A.; second harmonic generation was performed by J.X. under the supervision of X.Z.; electrical measurements were performed by S.S.C., N.S., and A.D.; S.S.C. and S.S. co-wrote the manuscript. S.S. supervised the research. All authors contributed to discussions and commented on the manuscript.

Competing Interests The authors declare no competing interests.

Additional Information

Reprints and permissions information is available at http://www.nature.com/ reprints

Correspondence and requests for materials should be addressed to S.S.C. (s.cheema@berkeley.edu) or S.S. (sayeef@berkeley.edu).

MAIN FIGURE LEGENDS

Figure 1 | Size effects in fluorite-structure ferroelectrics. a, In fluorite-structure ferroelectrics, the polar distortion present in the orthorhombic phase can be represented as the center anion displacement (cyan) with respect to its surrounding cation tetrahedron (represented by cyan arrow); in the nonpolar tetragonal phase, the oxygen atom (blue) lies in the polyhedral center of the tetrahedron. The evolution of the bulk-stable monoclinic polymorph to the high-symmetry tetragonal and polar orthorhombic phases in the fluorite-structure structure illustrates the role of size effects – surface energies favor higher symmetry – and confinement strain – distortions favor lower symmetry – on stabilizing inversion asymmetry. In fluorite-structures, the noncentrosymmetric O-phase is higher symmetry relative to the bulk-stable centrosymmetric M-phase. Consequently, both intrinsic (surface energy) and extrinsic (confinement strain) mechanisms can favor ultrathin inversion symmetry breaking in fluorite-structures, in stark contrast to size effect trends perovskites (Extended Data Fig. 1). **b,** Cross-sectional ADF STEM image of 20 cycle (~ 1.8 nm) HZO, demonstrating ultrathin HZO films on silicon via low-temperature ALD. The Si substrate is oriented along the [110] zone axis. **c,** Schematic heterostructure investigated in this work, detailing the ultrathin ferroelectric HZO layer deposited on Si/SiO_2, and the capping metal layer employed to impart confinement strain during post-deposition rapid thermal annealing (Methods).

Figure 2 | Electric polarization switching in ultrathin HZO. **a,** Schematic of the Si / SiO_2 (2 nm) / HZO (1 nm) heterostructure investigated by scanning probe imaging. **b,** Schematic of the HZO unit cell in the ferroelectric orthorhombic structure ($Pca2_1$). The different colored oxygen atoms represent the displaced oxygen atoms (cyan) and the centrosymmetric oxygen atoms (blue) within the surrounding cation tetrahedron. **c,** Microwave-frequency SCM spectroscopy for a 10 cycle HZO film. The presence of butterfly *C-V* conclusively demonstrates ferroelectricity in ultrathin HZO, enabled by the high-frequency detection of differential capacitance (Methods). Microwave *dC/dV* measurements on multiple regions of 10 cycles HZO demonstrate the robust ferroelectric behavior (Extended Data Fig. 8). **d,** Phase contrast PFM images demonstrating stable, bipolar, remnant polarization states that can be over-written into the opposite polarization state for

a 10 cycle HZO film. Note the unpoled outer perimeter matches phase contrast with the positively-poled regime regardless of the poling-polarity sequence; this indicates ultrathin HZO exhibits spontaneous polarization without requiring 'wake-up' effects to become ferroelectric. Time-dependent PFM imaging further demonstrates the robust ferroelectric contrast (Extended Data Fig. 7). **e,** Phase and amplitude switching spectroscopy (SS) loops for a 10 cycle HZO film, demonstrating ferroelectric-like hysteresis. Interferometry-based IDS PFM hysteresis loops confirm the origin of SS hysteresis is free of artifacts (Extended Data Fig. 7) and SS measurements demonstrating the critical role of confinement during phase annealing for stabilizing the polar phase in ultrathin HZO (Extended Data Fig. 6).

Figure 3 | Emergence of 'reverse' size effects in ultrathin HZO. **a,** Thickness-dependent XAS at the O *K*-edge; spectral weight XAS trends indicate enhanced polyhedral disorder and tetrahedral and rhombic distortions in ultrathin films, illustrated by the crystal field splitting diagram for the fluorite-structure structural polymorphs and symmetry-specific XAS simulations (Extended Data Fig. 9a,b). **b,** Thickness-dependent XLD at the O *K*-edge; the orbital polarization inversion below 25 cycles corresponds to the onset of highly-oriented ultrathin films. **c,** Thickness-dependent orbital polarization and XLD (inset) at the Zr M_2-edge. The orbital polarization trend indicates ultrathin-enhanced ZrO_4 tetrahedral distortion – schematically represented in **d)** by acentric oxygen atomic displacement (cyan atoms). **e,** Synchrotron GI-XRD demonstrating the emergence of highly-oriented ultrathin films, consistent with ADF-STEM (Fig. 1b) and pole figure analysis of ultrathin HZO (Extended Data Fig. 4b). **f,** Thickness-dependent GI-XRD around the polar orthorhombic (111) reflection, demonstrating a systematic shift in $2\theta_{111}$ with thickness, and highlighting the limitation of GI-XRD geometry to detect the (111)-reflection below 25 cycles as the film becomes highly-oriented (Extended Data Fig. 3). **g,** Thickness-dependent d_{111} lattice spacing and $^{2c}/_{a+b}$ structural aspect ratio, suggesting amplified polarization in the ultrathin limit, especially below 25 cycles. Dashed lines denote reported d_{111} and aspect ratio values for thicker ferroelectric HZO films. Aspect ratio values are extracted from the symmetry-split {200} planes (Methods).

METHODS

Sample deposition and preparation

Thin films of $Hf_{0.8}Zr_{0.2}O_2$ (HZO) were grown by atomic layer deposition (ALD) in a Fiji Ultratech/Cambridge Nanotech tool at 250°C in which tetrakis (ethylmethylamino) hafnium and tetrakis (ethylmethylamino) zirconium precursors are heated to 75°C and water vapor is used as the oxidant. For metal-ferroelectric-insulator-semiconductor (MFIS) structures, heavily p-doped Si(100) substrates ($10^{19}/cm^3$) are first oxidized in O_2 ambient during an RTA step at 900°C for 60 s, forming ~2 nm of thermal SiO_2 on Si. For metal-ferroelectric-metal (MFM) structures, the Si substrate is coated with 30 nm TiN. Subsequently, HZO is deposited at 250°C by ALD; a 4:1 ratio between the HfO_2 monolayer and the ZrO_2 monolayer sets the 80-20 stoichiometry of the deposited HZO, in which 10 cycles corresponds to one nanometer of film. After ALD deposition, a top metal (W or TiN) is deposited by sputtering at room temperature. Finally, a rapid post-metal annealing (PMA) at 500°C (30 s, ambient N_2 background) stabilizes the desired polar orthorhombic phase. For capacitor structures (scanning probe studies), the top electrodes are defined by photolithography and dry etching. For bare structures (structural studies), the top metal is removed by chemical etching to expose the HZO surface. Further details pertaining to ALD growth conditions, post-deposition processing, etc. are outlined in a previous work[42]. All thin film synthesis was performed at UC Berkeley; processing was performed at the UC Berkeley Marvell Nanofabrication Laboratory. 1 nm chemically-grown SiO_2 on Si was prepared by the standard clean (SC-1) solution (5:1:1 H_2O:H_2O_2:NH_4OH at 80°C for 10 minutes) after the Si wafer was cleaned in Piranha (120°C for 10 minutes) to remove organics and HF (50:1 H_2O:HF at room temperature for 30 s) to remove any native oxide. Thinner SiO_2 was employed to help reduce depolarization fields and improve the electric field distribution through the ultrathin ferroelectric HZO layer.

Electron microscopy

Electron microscopy was performed at the National Center for Electron Microscopy (NCEM) facility of the Molecular Foundry at LBNL as well as by Nanolab Technologies Inc., a commercial vendor. At NCEM, Transmission electron microscopy (TEM) samples were prepared by

mechanical polishing on an Allied High Tech Multiprep and subsequently Ar ion milled using a Gatan Precision Ion Milling System at shallow angles (5° to 3°) with starting energies of 5 keV stepped down to a final cleaning energy of 200 eV to reduce ion-induced damage. High-angle annular dark-field (HAADF) scanning transmission electron microscopy (STEM) images were recorded on TEAM I, an aberration-corrected FEI Titan 80–300 operated in STEM mode at 300 kV with a convergence semi-angle of 17 mrad, 70 pA probe current, and collection angles > 40 mrad. Local thicknesses of the respective HZO layers were determined from calibration to the Si(110) interplanar lattice spacing (Extended Data Fig. 3), consistent with global thicknesses extracted from x-ray reflectivity (Extended Data Fig. 2).

Scanning probe microscopy

Piezoresponse microscopy and spectroscopy Piezoresponse force microscopy (PFM) measurements (Extended Data Fig. 6, 7) were performed using a commercial scanning probe microscope (Asylum MFP-3D) at UC Berkeley. Dual a.c. resonance tracking (DART) PFM[43] was conducted using a conductive Pt/Ir-coated probe tip (NanoSensor PPP-EFM) to image written domain structures and measure switching-spectroscopy (SS)[44] piezoelectric hysteresis loops. Resonance-enhanced PFM increases the signal to noise ratio for the detection of out-of-plane electric polarization, critical for ultrathin films. Contact was made to the bottom TiN electrode or heavily doped Si substrate for grounding in PFM studies. All PFM phase contrast images and hysteresis loops shown were performed on 10 cycle (~ 1 nm) HZO films unless otherwise indicated. PFM imaging was performed with the tip in direct contact with the HZO layer. SS hysteresis loops were measured on capacitor structures to help eliminate electrostatic artifacts from the tip[45], mitigate possible electromechanical contributions[24], and to yield more confined electric fields. V_{ac}-dependent piezoresponse loops (Extended Data Fig. 7c) examined the ferroelectric origin of the PFM signal – as opposed to tip bias-induced artifacts[25] – in ultrathin HZO films. The piezoresponse (PR) "OFF" loop collapsed once V_{ac} exceeds the coercive voltage[46], as expected for ferroelectric behavior. Piezoresponse is defined as PR = $A \cdot \cos\theta$, where A and θ are the PFM amplitude and phase, respectively[45]. Note the non-ideal shape of the PR loops – particularly at higher voltages – are due to non-ferroelectric artifacts from the additional dielectric SiO_2 layer through which most of the voltage is dropped. For all PFM studies, the bias was applied to the tip.

Effective coercive field The switching voltage from PFM loops exaggerate the coercive field of the ultrathin HZO layer once considering the potential distribution across the modified metal-oxide-semiconductor (MOS) structure (oxide bilayer SiO_2-HZO). The effective coercive field of the HZO layer can be determined based on a simple dielectric-ferroelectric bilayer model, ignoring accumulation and depletion regions at the moment just to approximate the coercive field. Considering appropriate electrical boundary conditions across the oxide interface ($\epsilon_{DE} \cdot E_{DE} = \epsilon_{FE} \cdot E_{FE}$), the voltage across the ferroelectric layer (V_{FE}) can be expressed in terms of the total voltage given by the PFM loop (V_{tot}):

$$V_{FE} = \left(1 + \frac{t_{DE}}{t_{FE}} \frac{\epsilon_{FE}}{\epsilon_{DE}}\right)^{-1} \cdot V_{tot}$$

where the dielectric constant for the oxide layers are taken as ϵ_{DE}= 3.9 (SiO_2) and as ϵ_{FE}= 24 (HZO)[4,14] and the thicknesses of the oxide layers are t_{DE}= 2 nm and t_{FE} = 1 nm. These values yield $V_{FE} = V_{tot}/13$, so the effective coercive field of the 10 cycle (1 nm) ferroelectric HZO layer is approximately 2 MV/cm, consistent with values of thicker HZO films reported in literature[13].

Interferometry Interferometric displacement sensor (IDS) PFM measurements (Extended Data Fig. 7d) were performed using a commercial scanning probe microscope (Asylum Cypher) with an integrated quantitative Laser Doppler Vibrometer (LDV) at Asylum Research (Santa Barbara, CA). This recently developed method[26] eliminates crosstalk and other artifacts present in voltage-modulated piezo-measurements (d_{33}) by replacing the typical slope-sensitive optical beam detector (OBD) with a displacement sensitive interferometer. By positioning the IDS laser directly over the tip, motion of the tip can be decoupled from spurious motion of the cantilever body. Motion of the cantilever body can be driven by long range electrostatics and is influenced by the transfer function of the cantilever[26]. IDS measurements were performed with a 3 N/m Ti/Ir coated cantilever placed on the bare 1 nm HZO surface at 250 kHz drive frequency and 75 nN average force. Off-surface loops (tip raised from surface) – which measure the extrinsic electrostatic contributions[26] – were performed by changing the trigger value from deflection (force) to z-sensor read-out. The lack of hysteresis from off-surface (non-contact) loops further support the finding that the hysteresis observed from on-contact IDS measurements are free from electrostatic contributions. Typical voltage-modulated PFM measurements often display false ferroelectric

hysteresis due to long-range cantilever dynamics inherent to OBD detection, as observed from non-contact hysteresis in non-piezoelectric samples[26].

Microwave capacitance Scanning capacitance microscopy (SCM) measurements (Extended Data Fig. 8c) were performed using a commercial scanning probe microscope (Asylum Cypher) at Asylum Research (Santa Barbara, CA). Differential capacitance (*dC/dV*) measurements were performed at 1.8 GHz RF frequency with a 40 kHz lock-in frequency at 0.5 V_{ac}. Pure Pt cantilevers (Rocky Mountain Nanotechnology) are placed on top of bare HZO surface (contact mode) on TiN-buffered Si for SCM measurements; *dC/dV* signals were extracted via V_{ac} applied between the SCM tip and bottom electrode. *C-V* loops via SCM has been previously used to confirm ferroelectricity in $SrBi_2Ta_2O_9$ (SBT) thin films[47]. The microwave-frequency nature of the measurement lends itself to probing ultrathin ferroelectrics, as it mitigates leakage contributions. For SCM measurements, the bias was applied to the sample (swept up to ± 8 V), not the to tip as is done for PFM measurements.

X-ray diffraction

Structural characterization Synchrotron grazing-incidence x-ray diffraction (GI-XRD) (Extended Data Fig. 4a) was performed at Sector 33-BM-C beamline of the Advanced Photon Source, Argonne National Laboratory. Synchrotron GI-XRD investigated the structural evolution from polycrystalline bulk-like (100 cycles) HZO down to highly-textured ultrathin (< 25 cycles) HZO in its polar orthorhombic ($Pca2_1$) phase, at grazing angle $\leq \theta = 0.35°$. The high flux from the synchrotron source ($\lambda = 0.775$ Å) enabled collection of sufficient diffraction intensity from the few crystallographic planes present in ultrathin HZO samples. High-resolution GI-XRD was also performed using a laboratory-based Panalytical X'Pert Pro X-ray diffraction system (Cu K_α radiation, $\lambda = 1.54056$ Å) on HZO films thicker than 2 nm at grazing angle $\theta = 0.35°$. Previous work employed selected area electron diffraction (SAED)[48] and convergent beam electron diffraction (CBED)[49] to attribute ferroelectricity in HfO_2-based films to the polar orthorhombic ($Pca2_1$) phase. The indexing of ultrathin HZO films performed in this work is consistent with the same polar orthorhombic phase determined from these previous electron diffraction studies.

Texture analysis Pole figures (Extended Data Fig. 4b) were measured at Sector 33-BM-C beamline of the Advanced Photon Source, Argonne National Laboratory. For fixed Q values –

corresponding to the d_{111} lattice spacing – the 4-circle Huber diffractometer rotated in-plane (φ) 360° at multiple values of out-of-plane tilt (χ). The PILATUS 100K pixel area detector collected volumetric reciprocal space data from which 2D pole figure slices were plotted for shells of constant Q_z. The four concentrated reflections for the {111} projection in Q_x-Q_y space indicate highly-oriented texture, rather than diffuse rings expected for polycrystalline films. As indicated in the main text (Fig. 3), films thinner than 25 cycles display significant texturing (Extended Data Fig. 4); in particular, the (111) reflection, which is dominant for thicker films, is diminished in GI-XRD spectra of ultrathin films due to the geometric limitations of 1D pattern to detect all reflections present in oriented films. This limitation necessitates tilted geometry 2D patterns (pole figures) to detect all reflections present in highly-oriented films. Meanwhile, reflections corresponding to polycrystalline films exhibit continuous rings in 2D Q_x-Q_y reciprocal space, so any 1D line-cut (GI-XRD spectra) would detect all reflections present. The results on ultrathin HZO films are in stark contrast to results on thicker films[50,51] and indicates, that for such ultrathin films, crystallization and orientation need to be discussed together. We also observed that for such thin films, the template for HZO growth needs to be atomically smooth. Thus, the Si/SiO_2 interface employed in this work the growth surface is expected to play a more significant role for ultrathin films than for thicker films.

Thickness confirmation Synchrotron X-ray reflectivity (XRR) of ultrathin HZO films (Extended Data Fig. 2) – performed at Sector 33-BM-C beamline of the Advanced Photon Source, Argonne National Laboratory and at Beamline 2-1 of the Stanford Synchrotron Radiation Lightsource, SLAC National Accelerator Laboratory – confirmed the thickness of sub-2 nm films. Fitting analysis was performed with the python package xrayutilities[52]. XRR of thicker HZO films (> 2 nm) was measured with the Panalytical X'Pert Pro system, and thickness fitting was performed with Panalytical software. The extracted growth rate – 11 cycles/nm – is consistent with results from TEM and literature[13].

Structural distortion analysis For the polar orthorhombic phase ($Pca2_1$), we consider the orthorhombic distortion (i.e. orthorhombicity) as the aspect ratio: $2c/(a + b)$ to enable easier comparison to the tetragonal ($P4_2/nm$) aspect ratio c/a. fluorite-structure orthorhombicity is meant to draw analogies to the perovskite ferroelectric tetragonality (c/a, where c is the polar axis); both aspect ratios serve as a structural gauge of the macroscopic polarization as they are indicative of

the polar distortion present in their respective structures[53]. Notably, the orthorhombic distortion present in HZO is enhanced in the ultrathin regime – opposite to the typical tetragonal distortion trend in perovskite ferroelectrics[6] – indicative of the "reverse" size effects present in fluorite-structure ferroelectrics. For example, the tetragonal aspect ratio was shown to decrease with decreasing thickness in ferroelectric $PbTiO_3$ films[53], while the orthorhombic aspect ratio is significantly enhanced in the ultrathin regime in our fluorite-structure HZO films (Fig. 3g). The orthorhombic distortion present in 10 cycle (~ 1 nm) HZO far exceeds any reported values for HfO_2-ZrO_2 polymorphs: we find > 11% aspect asymmetry, while 3-4% is typically reported for fluorite-structure ferroelectrics[31], consistent with our thicker films (Fig. 3). Indeed, a strong relationship between this aspect ratio and remnant polarization value has been experimentally demonstrated in thicker doped-HfO_2 films[54]. Therefore, the colossal orthorhombic aspect ratio present in 10 cycle HZO is consistent with ultrathin-enhanced ferroelectricity. The orthorhombic aspect ratio is calculated from the position of various diffraction peaks indexed to the $Pca2_1$ phase – namely the 200-, 020, and 002- peaks – using the following crystallographic relations: $a = 2 \cdot d_{200}$, $b = 2 \cdot d_{020}$, $c = 2 \cdot d_{002}$ where d_{200}, d_{020}, and d_{002} are the 200-, 020-, and 002- lattice spacing determined via Bragg's law and the respective peak positions. These values are self-consistently checked against the 111- interplanar lattice spacing ($1/d_{111}^2 = 1/a^2 + 1/b^2 + 1/c^2$) as well as other orientations present in the diffraction spectra. The aspect ratio of the polar O-phase exceeds that of the T-phase (c/a) for doped-HfO_2[54]. Another structural marker indicates amplified distortions as thickness is reduced, namely the interplanar lattice spacing d_{111}. The origin of the left-shift in the O-phase 111 (T-phase 101) reflection (Fig. 3f) with decreasing thickness (i.e. decreasing ALD cycles) is typically attributed to the aforementioned phase transition (nonpolar T-phase to polar O-phase); the left-shift of the peak in reciprocal space corresponds to an increase in real-space lattice spacing. Extending this analogy to the ultrathin regime in which the polar O-phase is already stabilized, the ultrathin enhancement of d_{111} (Fig. 3g) indicates a further increase in rhombic distortion (structurally represented by d_{111}). Recent work on epitaxial HZO films grown by high-temperature pulsed laser deposition (PLD) on perovskite substrates also indicate increasing d_{111} with decreasing thickness[28,29]; these works find the electric polarization to increase with increasing d_{111}. Similarly, we expect a larger polarization in our ultrathin films based on the

d_{111} trend (Fig. 3g); notably, our low-temperature ALD-grown highly-oriented films are mimicking the trends observed in high-temperature PLD-grown epitaxial films.

X-ray spectroscopy

XAS and XLD X-ray absorption spectroscopy (XAS) and X-ray linear dichroism (XLD) was performed at the Advanced Light Source (ALS) beamline 4.0.2. XAS measurements were taken at the oxygen *K*-edge (520-550 eV) and Zr M_2-edge (345-355 eV). X-rays were incident at 20° off grazing. XLD (XAS) was obtained from the difference (average) of horizontal and vertical linearly polarized X-rays. To eliminate systematic artifacts in the signal that drift with time, spectra were captured with the order of polarization rotation reversed (e. g., horizontal, vertical, vertical, and horizontal) in successive scans. An elliptically polarizing undulator was used to tune polarization and photon energy of the synchrotron X-ray source[55]. XAS was recorded under total electron yield (TEY) mode[55].

Simulated XAS and crystal field symmetry Simulated XAS spectra for the various fluorite-structure polymorphs were computed through the Materials Project[56] open-source database for XAS spectrum[57]. In particular, the following symmetries for HfO_2 and ZrO_2 were investigated: monoclinic $P2_1/c$ (space group 14), orthorhombic $Pca2_1$ (space group 29), and tetragonal $P4_2/nmc$ (space group 137). Comparisons between HZO and the undoped fluorite-structure end-members – in particular, qualitative comparison of splitting-induced spectroscopy features – are reasonable due to the extremely low structural dissimilarity between the same polymorphs of HfO_2 and ZrO_2, as determined by pymatgen[58]. The T-phase ($P4_2/nmc$) nonpolar distortion (D_{4h}, 4-fold prismatic symmetry) from regular tetrahedral (T_d, full tetrahedral symmetry) fluorite-structure symmetry does not split the degenerate *e*-bands ($d_x2_{-y}2$, $d_{3z}2_{-r}2$), as confirmed by experiment[59] and the XAS simulations (Extended Data Fig. 9b). Meanwhile, the O-phase ($Pca2_1$) polar rhombic pyramidal distortion (C_{2v}, 2-fold pyramidal symmetry) does split the *e*-manifold based on crystal field symmetry (Extended Data Fig. 9b), providing a spectroscopic means to distinguish the T- and O-phases. The eight-fold Hf-O (Zr-O) coordination (Extended Data Fig. 9d) in the tetragonal phase (D_{2d} point group symmetry) can be decomposed into two tetrahedra which are the space inversion twins of one another. Therefore, crystal field splitting of the *e*-levels matches that of a single tetrahedron[59] i.e. there is no further splitting. Meanwhile, the seven-fold Hf-O (Zr-O) coordination

(Extended Data Figure 9d) in the orthorhombic phase cannot be decomposed into two tetrahedra; the additional rhombic distortion (not present in the T-phase) splits the *e*-manifold. The simulated XAS spectra for T- and O-phase ZrO_2 (Extended Data Fig. 9b) supports this picture, as the additional spectroscopic feature present between the main *e*- and t_2- absorption features in the O-phase is presumably due to this additional symmetry-lowering distortion. The XAS spectra of the HZO thickness series (Extended Data Fig. 9c) demonstrates tetrahedral and rhombic splitting features closely matching the polar O-phase ($Pca2_1$). This demonstrates a spectroscopic method for phase identification beyond diffraction – ambiguous due to the nearly identical T- and O-phase lattice parameters[13] – whose signatures are more sensitive to the subtle structural distortions present as symmetry is lowered from the T- to the O-phase.

Crystal field splitting Notably, the crystal field distortions present in confined HZO films greatly exceed what is typically observed in bulk fluorite-structures and perovskite ferroelectrics (Extended Data Fig. 9g); the tetrahedral (rhombic) crystal field Δ_T (Δ_R) arising from the T_d (C_{2v}) symmetry in 10 cycle HZO films is 1.3 eV (0.7 eV) greater than what is expected from fluorite-structure ZrO_2 in the polar orthorhombic phase ($Pca2_1$). The computational XAS for the $Pca2_1$ phase already takes the polar distortion (Δ_R) into account; therefore, the enhanced Δ_R in ultrathin confined films again points to enhanced polar distortions (consistent with diffraction-based results). Kindred efforts to unravel novel routes towards enhanced nanoscale distortions have been explored in complex perovskite heterostructures. For example, in nickelate perovskite superlattices, enormous Δ_{eg} crystal field splitting (up to 0.8 eV) has been achieved via polar fields resulting from internal charge transfer[27]; > 10% epitaxial strain would be required to induced such large ionic distortions in that particular system, well beyond the limits epitaxial strain, which can only achieve e_g splitting ~300 meV [60].

Spectral weight trends The relative spectral weight of the *e* and t_2 manifolds (Extended Data Fig. 9c) at the O *K*-edge can also provide insight into the degree of structural distortion[61]. Due to the d^0 electronic configuration present in Hf^{4+} (Zr^{4+}), all *d* states are available for mixing with O 2*p* states; therefore, the analysis of *e*-t_2 spectral weight can be simplified to be purely due to crystal field effects[61]. Tetrahedral symmetry lowers *e* bands relative to t_2 bands due to enhanced t_2 orbital overlap with oxygen 2*p* orbitals. The enhanced t_2/*e* spectral weight as thickness is reduced (Extended Data Fig. 9c) indicates the preference for O 2*p* hybridization with Hf 5*d* (Zr 4*d*) t_2

orbitals, further exaggerating the disparity set by the tetrahedral symmetry as the symmetry is lowered to the polar O-phase. Additionally, the increase in spectral weight of the pre-edge shoulder (Extended Data Fig. 9e) provides further confirmation that structural distortions are amplified in the ultrathin limit. Pre-edge features at the O *K*-edge in complex transition metal oxides are commonly attributed to nearest neighbor (NN) variations from typical oxygen polyhedral coordination as the symmetry is lowered by various distortions[62]. Analogously, here the pre-edge feature is attributed to variation from 8-fold coordination in the T-phase (NN=8) as the symmetry is lowered into the polar O-phase (NN=7) (Extended Data Fig. 9d). On the unit cell level in the polar O-phase, the central metal cation is surrounded by an asymmetric oxygen coordination environment (note the 4 blue and 3 cyan oxygen atoms in Extended Data Fig. 1d) due to the polar rhombic distortion of normal tetrahedral (T_d) symmetry; this polyhedral distortion can manifest as increased spectral weight at the oxygen *K* pre-edge[62]. The critical *e*-manifold splitting due to the polar rhombic distortion also increases in spectral weight as thickness is reduced (Extended Data Fig. 9c). The XAS spectral weight trends mirror the structural indicators of ultrathin-enhanced distortion (Fig. 3c).

Orbital polarization In conjunction with XAS, X-ray linear dichroism (XLD) can also probe structural distortions due to its sensitivity to orbital asymmetry, which can arise from inversion symmetry breaking. For example, in perovskite ferroelectrics $PbTiO_3$ and $BaTiO_3$, the Ti 3*d* - O 2*p* orbital hybridization is essential for stabilizing the noncentrosymmetric structure[63]. Particularly at the 3*d* cation $L_{3,2}$ edge, orbital polarization extracted from XLD is used as a measure of the oxygen octahedral distortion in perovskites due to the anisotropic hybridization between cation 3*d* and O 2*p* orbitals[64]. Accordingly, in fluorite-structure ferroelectrics, the magnitude of XLD present at the Zr $M_{3,2}$ edges can be a gauge of the degree of polyhedral distortion – in this case distortion of oxygen tetrahedron – and the oxygen atomic asymmetry. Indeed, the orbital polarization at the Zr M_2-edge is enhanced as the thickness is reduced from the thick (100 cycles) to ultrathin (10 cycles) regime (Fig. 3c), consistent with diffraction-based results demonstrating amplified structural distortions in the ultrathin limit. Spectroscopy can also help understand the evolution to highly-textured films in the ultrathin limit (Fig. 3e-f), as XLD enables both element- and orbital-specific information by comparing polarization-dependent XAS spectra. GI-XRD across the thickness series (Fig. 3f) indicates the degree of orientation significantly changes as the HZO drops

below ~2.5 nm (25 cycles). The microstructure change below 25 cycles also manifests as inverted orbital polarization at the oxygen *K*-edge, particularly at the *e*-manifold (Fig. 3b). Absorption of vertically and horizontally polarized light preferentially probe the polar-distortion-split *e*-levels (x^2y^2 and $3z^2r^2$ orbitals); the reversal of XLD sign indicates these levels are inverted with respect to one another. In perovskites, such a change orbital polarization is often attributed to different signs of tetragonal distortion (*c/a*) of oxygen octahedron[64]. Analogously, here the change in microstructure across 20-25 cycles – namely the emergence of highly-oriented films – could allow confinement strain effects to more coherently distort the oxygen tetrahedron along the polar axis. This synergistic effect could potentially explain the enhanced distortions observed in the ultrathin regime.

Nanospectroscopy Photoemission electron microscopy (PEEM) was performed at the Advanced Light Source (ALS) beamline 11.0.1. X-rays were incident at 30° off grazing, probing just the first few nanometers of film, spanning the entire 10 cycle (1 nm) HZO thickness. Nanospectroscopy point-by-point scans were employed to spatially resolve XLD contrast; at each specified energy value in the oxygen *K*-edge (520-550 eV) regime, PEEM images were taken for both values of the linear polarization (horizontal, vertical) across a 20 μm field-of-view (1000 x 1000 pixel grid). The exposure to high-flux synchrotron x-rays likely depolarized the ultrathin ferroelectric sample as photoelectrons were removed from the surface, as is observed in ultrathin films of $BaTiO_3$ and other ferroelectrics; PEEM-XLD images (Extended Data Fig. 9f) illustrate nanoscale domains at the energy range corresponding to the polar *e*-split feature. Data processing to extract XLD contrast involved diving images of opposite linear polarization, which eliminates topography and work function contrast. Topography and work function artifacts contribute at the pre-edge (~530 eV), while the intrinsic orbital anisotropy contributions only manifest at resonance (~535 eV); the presence of XLD contrast only at resonance confirms the orbital asymmetry origins of XLD contrast in ultrathin HZO. Furthermore, the highly-textured nature of the ultrathin films prevents the XLD contrast from averaging to zero – cancellation would be expected for a fully polycrystalline film – on a length scale smaller than the experimental resolution.

Optical spectroscopy

SHG and inversion asymmetry Nonlinear optical second harmonic generation (SHG) was performed using a custom setup at UC Berkeley, detailed in a previous work[23]. The excitation light was extracted using an optical parametric oscillator (Inspire HF 100, Spectra Physics, Santa Clara, USA) pumped by a mode-locked Ti:sapphire oscillator. The excitation laser was linearly polarized by a 900–1300 nm polarizing beamsplitter. The transmitted *p* polarized laser light can change its polarization by rotating a IR half waveplate before pumping sample. The laser is focused by a 50x NIR objective on sample. The second harmonic generation signal was detected in the backscattering configuration, analyzed by a visible-range polarizer, and finally collected by a cooled CCD spectrometer. SHG was performed with a 960 nm pump and detected at 480 nm under tilt incidence. SHG is commonly used to investigate piezoelectric and ferroelectric single crystals and thin films[65] as the photon frequency-doubling process is allowed only in materials lacking inversion symmetry.

Field-dependent SHG Electric field-dependent SHG experiments were performed on the bare surface of 10 cycle (1 nm) HZO films (top metal was etched away after phase annealing). The HZO layer was then patterned into micron-sized islands to enable systematic identification of specific HZO regions; various islands were poled with an electric field (applied by a PFM tip), while other islands were left as-is. The optical microscope identified the poled and unpoled islands, and the second harmonic signal was detected across various islands. Increased SHG intensity – sensitive to out-of-plane polarization is this tilt-incidence experimental geometry – in poled HZO islands suggests the electric field increases the projection of out-of-plane polarization by aligning domains with different polarization directions.

Electrical characterization

Tunnel current measurements Tunnel current measurements were performed using a commercial Semiconductor Device Analyzer (Agilent B1500) with a pulse generator unit (SPGU) to enable voltage pulses down to the microsecond regime. Samples were patterned into capacitors of various area, with W as the top electrode, and heavily doped Si (10^{19} cm^{-3}) as the bottom contact. 19 μm W tips (DCP-HTR 154-001, FormFactor) made electrical contact within a commercial probe station (Cascade Microtech). In tandem, conducting atomic force microscopy (CAFM) measurements were performed using a commercial scanning probe microscope (Asylum MFP-3D)

at UC Berkeley. I-V characteristics through the capacitor device were probed in the AFM by using a Keithley 2400 Source Measure Unit (SMU) to bias the top electrode of the sample through 20 nm radii Pt/Ir-coated AFM probes (25PtIr300B cantilever probe, Rocky Mountain Nanotechnology), grounded to the heavily-doped Si substrate.

IV hysteresis and tunnel electroresistance Voltage polarity-dependent I-V hysteresis was employed to rule out resistive switching mediated by dielectric breakdown and filamentary-type switching. For filamentary-mediated resistive switching – often observed in amorphous HfO_2 – the sense of hysteresis is dependent on the direction of the voltage sweep (i.e. initial polarity of the voltage waveform) which dictates the filament formation[66]. Meanwhile, ferroelectric tunnel junctions demonstrate the same sense of IV hysteresis independent of the sweep direction; this voltage polarity-independence is indicative of polarization-mediated switching, as observed for our ultrathin 10 cycle (1 nm) HZO films (Extended Data Fig. 10). To further investigate the origin of the resistive switching, tunneling electroresistance (TER) hysteresis maps as a function of write voltage (at low read voltage) demonstrate saturating, abrupt hysteretic behavior (Extended Data Fig. 10) characteristic of polarization-driven switching[67,68]. TER evidence of polarization-driven resistive switching is provided for 10 cycle (1 nm) HZO films of two different compositions (Extended Data Figure 10). Although much of the results presented in this paper are on films with 4:1 Hf:Zr ratio, for comparison, we have included results and demonstrated ferroelectricity for a 10 cycle (1 nm) film with this modified 1:1 Hf:Zr ratio. Pioneering work on HZO in the thicker regime (> 5 nm)[50,69,70] have shown that 1:1 Hf:Zr ratio often demonstrate the best ferroelectric properties. Ferroelectric tunnel junctions based on composite ferroelectric-dielectric barriers utilizing HZO in this thicker regime demonstrate promising polarization-driven resistive switching results[71,72]. Optimizing FTJ behavior employing HZO the ultrathin regime (~ 1 nm) will need to be carefully studied.

METHOD REFERENCES

42. Karbasian, G. *et al.* Stabilization of ferroelectric phase in tungsten capped $Hf_{0.8}Zr_{0.2}O_2$. *Appl. Phys. Lett.* 111, 022907 (2017).
43. Rodriguez, B. J., Callahan, C., Kalinin, S. V. & Proksch, R. Dual-frequency resonance-tracking atomic force microscopy. *Nanotechnology* 18, 475504 (2007).
44. Jesse, S., Lee, H. N. & Kalinin, S. V. Quantitative mapping of switching behavior in piezoresponse force microscopy. *Rev. Sci. Instr.* 77, 073702 (2006).
45. Hong, S. *et al.* Principle of ferroelectric domain imaging using atomic force microscope. *J. Appl. Phys.* 89, 1377–1386 (2001).
46. Strelcov, E. *et al.* Role of measurement voltage on hysteresis loop shape in piezoresponse force microscopy. *Appl. Phys. Lett.* 101, 192902 (2012).
47. Leu, C.-C. *et al.* Domain structure study of $SrBi_2Ta_2O_9$ ferroelectric thin films by scanning capacitance microscopy. *Appl. Phys. Lett.* 82, 3493–3495 (2003).
48. Chernikova, A. *et al*. Ultrathin $Hf_{0.5}Zr_{0.5}O_2$ Ferroelectric Films on Si. *ACS Appl. Mater. Interfaces* 8, 7232–7237 (2016).
49. Sang, X., Grimley, E. D., Schenk, T., Schroeder, U. & LeBeau, J. M. On the structural origins of ferroelectricity in HfO_2 thin films. *Appl. Phys. Lett*.106, 162905 (2015).
50. Böscke, T. *Crystalline Hafnia and Zirconia Based Dielectrics for Memory Applications*. Ph.D. thesis (2010).
51. Zhao, C., Roebben, G., Heyns, M. M. & Van der Biest, O. Crystallisation and Tetragonal-Monoclinic Transformation in ZrO_2 and HfO_2 Dielectric Thin Films. *Key Eng. Mater.* 206-213, 1285–1288 (2001).
52. Kriegner, D., Wintersberger, E. & Stangl, J. xrayutilities: a versatile tool for reciprocal space conversion of scattering data recorded with linear and area detectors. *J. Appl. Crystallog.* 46, 1162–1170 (2013).
53. Lichtensteiger, C., Triscone, J., Junquera, J. & Ghosez, P. Ferroelectricity and Tetragonality in Ultrathin $PbTiO_3$ Films. *Phys. Rev. Lett.* 94, 047603 (2005).
54. Park, M. H. *et al.* A comprehensive study on the structural evolution of HfO_2 thin films doped with various dopants. *J. Mater. Chem. C* 5, 4677–4690 (2017).
55. Young, A. T. *et al.* Variable linear polarization from an x-ray undulator. *J. Synch. Rad.* 9, 270–4 (2002).
56. Jain, A. *et al.* The materials project: A materials genome approach to accelerating materials innovation. *APL Mater.* 1, 011002 (2013).
57. Mathew, K. *et al.* High-throughput computational X-ray absorption spectroscopy. *Sci. Data* 5, 180151 (2018).
58. Ong, S. P. *et al.* Python materials genomics (pymatgen): A robust, open-source python library for materials analysis. *Comput. Mater. Sci.* 68, 314–319 (2013).
59. Cho, D.-Y., Jung, H.-S. & Hwang, C. S. Structural properties and electronic structure of HfO_2-ZrO_2 composite films. *Phys. Rev. B* 82, 094104 (2010).
60. Wu, M. *et al.* Strain and composition dependence of orbital polarization in nickel oxide superlattices. *Phys. Rev. B* 88 (2013).
61. De Groot, F. *et al.* Oxygen 1s X-ray-absorption edges of transition-metal oxides. *Phys. Rev. B* 40, 5715–5723 (1989).

62. De Groot, F. Multiplet effects in X-ray spectroscopy. *Coord. Chem. Rev.* 249, 31–63 (2005).
63. Cohen, R. E. Origin of ferroelectricity in perovskite oxides. *Nature* 358, 136–138 (1992).
64. Fontcuberta, J. *et al.* Surface symmetry-breaking and strain effects on orbital occupancy in transition metal perovskite epitaxial films. *Nat. Commun.* 3, 1189 (2012).
65. Denev, S. A., Lummen, T. T. A., Barnes, E., Kumar, A. & Gopalan, V. Probing Ferroelectrics Using Optical Second Harmonic Generation. *J. Am. Ceram. Soc.* 94, 2699–2727 (2011).
66. Bersuker, G. & Gilmer, D. Metal oxide resistive random-access memory (RRAM) technology. In *Advances in Non-Volatile Memory and Storage Technology*, 288–340 (Elsevier, 2014).
67. Chanthbouala, A. *et al.* Solid-state memories based on ferroelectric tunnel junctions. *Nat. Nanotechnol.* 7, 101–104 (2012).
68. Gruverman, A. *et al.* Tunneling Electroresistance Effect in Ferroelectric Tunnel Junctions at the Nanoscale. *Nano Lett.* 9, 3539–3543 (2009).
69. Müller, J. *et al.* Ferroelectricity in Simple Binary ZrO_2 and HfO_2. *Nano Lett.* 12, 4318–4323 (2012).
70. Park, M. H. *et al.* Surface and grain boundary energy as the key enabler of ferroelectricity in nanoscale hafnia-zirconia: a comparison of model and experiment. *Nanoscale* 9, 9973–9986 (2017).
71. Fujii, S. *et al.* First demonstration and performance improvement of ferroelectric HfO_2-based resistive switch with low operation current and intrinsic diode property. In *2016 IEEE Symposium on VLSI Technology*, 1–2 (IEEE, 2016).
72. Max, B., Hoffmann, M., Slesazeck, S. & Mikolajick, T. Ferroelectric Tunnel Junctions based on Ferroelectric-Dielectric $Hf_{0.5}Zr_{0.5}O_2/Al_2O_3$ Capacitor Stacks. In *2018 48th European Solid-State Device Research Conference (ESSDERC)*, 142–145 (IEEE, 2018).

Data Availability

The datasets generated during and/or analyzed during the current study are available from the corresponding author on reasonable request.

EXTENDED DATA FIGURE LEGENDS

Extended Data Figure 1 | Size effects in fluorite- and perovskite-structure ferroelectrics. **a,** In perovskite ferroelectrics, the polar "tetragonal" distortion (c/a) can be represented as the center cation displacement with respect to its surrounding oxygen octahedron. **b,** In fluorite-structure ferroelectrics, the polar "rhombic" distortion ($2c/(a+b)$) can be represented as the center anion displacement with respect to its surrounding cation tetrahedron; in the nonpolar T-phase, the oxygen atom (blue) lies in the polyhedral center of the tetrahedron. The evolution of the bulk-stable M-phase to the high-symmetry T-phase and polar O-phase in the fluorite-structure structure illustrates the role of size effects – surface energies favor higher symmetry – and confinement strain – distortions favor lower symmetry – on stabilizing inversion asymmetry. Surface energies are critical when considering the role of size effects on ferroelectricity; higher symmetry phases are energetically favorable at reduced dimensions due to lower unit cell volumes. In fluorite-structures (perovskites), the noncentrosymmetric O-phase (T-phase) is higher (lower) symmetry relative to the bulk-stable centrosymmetric M-phase (C-phase). Consequently, surface energies help counteract depolarization fields in fluorite-structure ferroelectrics – already diminished in fluorite-structures relative to perovskites due its lower dielectric constant[4] – in the ultrathin regime. Therefore, both intrinsic (surface energies) and extrinsic (confinement strain) mechanisms can favor ultrathin inversion symmetry breaking in fluorite-structures. Meanwhile, both surface and depolarization energies tend to destabilize inversion asymmetry in perovskite ferroelectrics, while epitaxial strain can stabilize symmetry-lowering polar distortions. Italic font represents the bulk stable phase, and blue font indicates the polar phase.

Extended Data Figure 2 | Thickness verification of ultrathin HZO films from x-ray reflectivity. **a,** Laboratory diffractometer XRR of HZO thickness series, demonstrating clear fringes for thickness extraction present down to 20 cycles HZO. **b,** Synchrotron XRR of ultrathin HZO films, enabling thickness fitting analysis for sub-20 cycle films. **c,** HZO thickness as a function of ALD cycles, as determined by fitting analysis from XRR. The growth rate is ~ 11 cycles / nm, verified across 10 - 100 ALD cycle films. Squares (circles) represent thicknesses extracted from fitting to synchrotron (laboratory diffractometer) XRR measurements.

Extended Data Figure 3 | Thickness verification of ultrathin HZO films from transmission electron microscopy. **a,** HZO thickness as a function of ALD cycles, as determined by Si atomic lattice calibration from TEM imaging. The growth rate is ~ 11 cycles / nm, verified across 10 - 50 ALD cycle films, consistent with x-ray reflectivity (Extended Data Fig. 2). The red error bars reflect 2σ variation. **b,** Cross-sectional ADF STEM image of 20 cycles HZO. **c, d, e,** Cross-section TEM images of 10 cycles HZO **(c)**, 15 cycles HZO **(d)** and 40 cycles HZO **(e)**. **f, g, h,** Wide field-of-view TEM images of 10 cycles HZO **(f)**, 15 cycles HZO **(g)** and 40 cycles HZO **(h)** to provide perspective of the heterostructure uniformity. The Si substrate is oriented along the [110] zone axis for all TEM images.

Extended Data Figure 4 | Emergence of highly-textured films in the ultrathin regime. **a,** Synchrotron GI-XRD scans (λ = 0.775 Å) of HZO thickness series endmembers: 10 cycles and 100 cycles. The 100 cycle HZO film is indexed according to the polar orthorhombic phase $Pca2_1$. Many of the polycrystalline reflections – most notably the (111) – are no longer present at an appreciable intensity in the ultrathin limit due to the geometric constraint of 1D spectra to probe all reflections present in highly-oriented films (Methods). Instead tilted-geometry diffraction (pole figures) are used to access the oriented reflections. **b,** Pole figure of 10 cycles HZO, taken at a Q_x slice corresponding to the film (111) lattice spacing. The radial direction represents χ, while the azimuthal direction represents φ (0°-360° range). The presence of four intense peaks corresponding to the four (111)-projections indicate the highly-textured nature of the ultrathin HZO film. The four Si (111)-projections would be expected at φ = 45° off from the $Q_{x,y}$ principle axes at a smaller value of Q_z. **c,** Left and right: Schematic of the (311) and (111) close-packed planes (CPP) in the fluorite-structure structure. All the cation sites lie on such planes, which minimize surface energy effects as only metal-oxygen dangling bonds are present out-of-plane. Note: all schematics reflect stacking of the respective planes to total 1 nm thickness, although ultrathin HZO films may not exhibit such stacking throughout the film. For 10 cycle films, {311} indexing is consistent with the significant intensity (~30°) observed in the out-of-plane 1D GI-XRD pattern **(a)**, and the (111) reflections are present from the 2D pole figure pattern **(b)**.

Extended Data Figure 5 | Inversion symmetry breaking in ultrathin HZO via second harmonic generation. **a,** Schematic of the SHG experimental setup, using a 960 nm pump and

SHG intensity detected around 480 nm under tilt incidence, which is sensitive to out-of-plane polarization (Methods). **b,** Schematic of the 10 cycle HZO islands probed by SHG (Methods); micron-sized islands enabled identification of specific HZO regions either poled with an electric field (applied by a PFM tip) or left as-is. **c,** Second harmonic generation (SHG) spectrum on a 10 cycles HZO film, comparing poled versus unpoled SHG intensity. Spontaneous polarization is demonstrated by the presence of second harmonic generation (SHG) – allowed only for inversion asymmetric systems – in unpoled 10 cycles HZO. This is consistent with PFM phase contrast in unpoled HZO regions (Fig. 2c), indicating elimination of "wake-up" effects for ferroelectricity in ultrathin HZO. The enhanced SHG contrast in poled films – possibly due to the electric field converting a small fraction of the film to the polar phase or aligning polar domains – indicates the mechanism behind the SHG contrast is field-tunable. This field-enhanced SHG is consistent with ferroelectric origins and would likely eliminate SHG contrast from surface effects.

Extended Data Figure 6 | Role of ultrathin confinement for polar phase stabilization. **a, b,** Schematic structure (left) probed by PFM (tip location indicated by arrows), topography (center), and PFM phase contrast images (right) on 10 cycles HZO in a region that was uncapped **(a)** versus confined **(b)** by W during phase annealing. Robust 180° phase contrast is only present for the confined HZO. **c,** Phase (left) and amplitude (right) switching spectroscopy loops ($V_{dc} = 0$, 'OFF' state) on 10 cycle HZO films, demonstrating the critical role of confinement during phase annealing for stabilizing ferroelectricity in ultrathin HZO. 180° phase contrast and butterfly-shape amplitude are only present for confined HZO. Therefore, both SS-PFM and PFM imaging illustrate the critical role of confinement during phase annealing for stabilizing the ferroelectric phase. For the PFM images, ± 7 V were applied in a "box-in-box" poling pattern directly on the HZO surface, and SS-PFM loops were measured on capacitor structures (Methods). **d,** Schematic structure (left) probed by PFM (tip location indicated by arrows) and PFM phase and amplitude hysteresis loops (right) on 100 cycles HZO in a region that was confined by W during phase annealing. Thicker 100 cycles HZO also demonstrates ferroelectric behavior.

Extended Data Figure 7 | Eliminating artifacts from scanning probe microscopy. **a,** Topography and PFM phase contrast images for 10 cycles HZO which did not (left) and did (right)

undergo annealing after ALD deposition. The terraced topography in the non-annealed film indicates that the weak phase contrast is falsely due to field-induced topographic changes. This is consistent with charge injection or ion migration which plague amorphous HfO_2 films[25]. Phase annealed films do not display such field-induced topographic distortions yet demonstrate much clearer phase contrast, indicating the origin of PFM phase contrast in crystalline HZO films is different than that of amorphous HZO films. In the images shown, ± 7 V were applied in a 'box-in-box' poling sequence. **b,** Time-dependent PFM phase contrast images on a 10 cycles HZO film across a 24 hour period. In the images shown, ± 7 V were applied in the indicated checkerboard poling pattern. **c,** Collapse of the PFM loop from V_{ac}-series. Schematic capacitor structure probed by PFM (top) and piezoresponse (PR) as a function of V_{ac} in the 'OFF' (V_{dc}=0) state (bottom), demonstrating the collapse of the PFM loop as V_{ac} approaches the coercive voltage. This provides further confirmation of the ferroelectric-origin of the PFM signal as opposed to tip bias-induced mechanisms[46]. The non-ideal shape of the PR loops – particularly at higher voltages – are likely due to non-ferroelectric contributions from the additional dielectric SiO_2 layer through which most of the voltage is dropped (Methods). **d,** IDS switching spectroscopy (SS) measurements on 10 cycle (1 nm) HZO, demonstrating hysteresis for the PFM tip on-surface (top) versus no hysteresis for the tip off-surface (bottom). The on-surface loops indicate 180° phase hysteresis and butterfly-shape d_{33}, indicative of ferroelectric behavior. IDS-PFM measurements (Methods) remove long-range electrostatics and cantilever resonance artifacts which plague typical voltage-modulated PFM SS[26]. This ferroelectric origin of the hysteresis is further supported by non-hysteretic off-surface loops[26] which probe electrostatic contributions.

Extended Data Figure 8 | High-frequency capacitance characterization of ultrathin HZO. **a,** Schematic heterostructure of ultrathin HZO on metallic TiN probed the microwave capacitance measurements to eliminate contributions from the semiconducting Si substrate. **b,** PFM phase contrast and topography imaging for 10 cycles HZO on TiN-buffered Si. Ultrathin ferroelectricity persists on top of metallic underlayers as well as dielectric SiO_2, although the topography is rougher than the films on SiO_2 due to the inhomogeneity introduced by the sputtered TiN. **c,** Scanning capacitance microscopy (SCM) *dC-dV* spectroscopy loops taken on multiple bare regions of an ultrathin 10 cycle HZO film, demonstrating reproducible SCM response. The square 180°

phase hysteresis and *dC/dV* loops – which integrates into the classic butterfly-shape *C-V* (Fig. 2c) – provides conclusive evidence of ferroelectric polarization switching beyond PFM loops (Fig. 2e, Extended Data Fig. 6). The microwave-frequency nature of the SCM enables leakage-mitigated differential capacitance measurements of ultrathin films (Methods). **d,** PFM SS loops taken on the same region of the 10 cycles HZO as the SCM measurements, confirming ferroelectric-like phase and amplitude hysteresis. Note the SCM and PFM SS were collected using the Asylum Cypher scanning probe microscope at Asylum Research (Methods).

Extended Data Figure 9 | Ultrathin-enhanced distortions and polar signatures from spectroscopy. **a,** Crystal field splitting diagram for the fluorite-structure structural polymorphs; symmetry-induced *e*-splitting provides a spectroscopic signature for the polar O-phase (Methods). **b,** Delineating symmetry-split energy regimes in oxygen *K*-edge XAS. Just as CBED provides signatures to demonstrate inversion symmetry breaking, XAS provides spectroscopic signatures to distinguish between the nonpolar tetragonal and polar orthorhombic polymorphs (difficult to resolve from GIXRD). Shown are (left) simulated XAS spectrum for tetragonal ZrO_2 ($P4_2/nmc$) and (right) polar orthorhombic ZrO_2 ($Pca2_1$), courtesy of the Materials Project[55]. The background color shading denotes symmetry-split regimes explained in the crystal field splitting diagram, **c,** Experimental XAS data on ultrathin HZO displays similar spectroscopic XAS features as the simulated polar O-phase ($Pca2_1$) – namely relative e/t_2 spectral weight and splittings corresponding to tetrahedral (Δ_T) and rhombic (Δ_R) distortions. Left: XAS of the HZO thickness series at the O *K*-edge, zooming in on the *e*- and t_2-regimes. Right: O *K*-edge spectral weight trends as a function of HZO thickness. The relative spectral weight from the t_2/e- *e*-split regimes the indicate enhanced tetrahedral (Δ_T) and rhombic distortions (Δ_R) in ultrathin films, respectively, consistent with C_{2v} symmetry of the polar O-phase. **d,** Schematic representation of the cation nearest neighbor (NN) coordination lowering from NN = 8 (T-phase) to NN = 7 (polar O-phase) as the crystal symmetry is lowered. The disorder in oxygen polyhedral coordination – note the different oxygen atoms denoted by the blue and cyan atoms in the polar O-phase – manifests as spectral weight in the pre-edge regime[60]. **e,** The experimental pre-edge spectral weight as a function of thickness, indicating ultrathin-enhanced polyhedral disorder. **f,** Top: PEEM-XLD images of 10 cycle (1 nm) HZO at the O *K*-edge. Pre-edge images (left) exhibit no XLD contrast, while on-edge images (right) – at the

energy corresponding to the polar-distortion split *e*-regime – demonstrate XLD contrast. This suggests XLD is indeed sensitive to polar features in ultrathin highly-textured HZO. Bottom: Line profile of the XLD intensity demonstrating statistically significant variations in on-edge XLD data compared to noise for pre-edge XLD. **g,** Crystal field splitting energies in HZO-related transition metal oxide systems. Material system, primary crystal electric field (Δ_1), secondary crystal electric field (Δ_2), and structure for various systems related to HZO and perovskite ferroelectrics, where Δ_O, Δ_t, Δ_T, Δ_R corresponds to octahedral, tetragonal, tetrahedral, and rhombic crystal electric field (CEF), respectively. The reference CEF values are taken from the Materials Project database[55] (reference codes denoted by "mp"), and the experimental values are extracted via XAS energy-split features **(b)**. The large tetrahedral (Δ_T) and rhombic (Δ_R) crystal field splitting energies present in 10 cycle HZO films are significantly larger than expected values for the polar fluorite-structure ZrO_2 **(b)**, which highlights the enhanced distortion present in ultrathin films subject to confinement strain, and is consistent with anomalously large structural distortions extracted from diffraction (Fig. 3g).

Extended Data Figure 10 | Ultrathin HZO ferroelectric tunnel junction. **a, b,** Tunnel current-voltage (*I-V*) characterization of Si(p^{++})/SiO_2(1 nm)/HZO(∼1 nm)/W capacitor devices – demonstrated for 10 cycles HZO with Hf:Zr composition 4:1 **(a)** and 1:1 **(b)** – as a function of write pulse (to set the ferroelectric polarization state). Tunneling electroresistance (TER) behavior is demonstrated for ± 2 V write and 100 mV read. Inset: Linear scale I-V characteristics of the two polarization-driven current states. **c, d,** TER hysteresis map as a function of write voltage – demonstrated for 10 cycles HZO with Hf:Zr composition 4:1 **(c)** and 1:1 (**d)** – measured at 200 mV read voltage. The abrupt hysteretic behavior and saturating TER is characteristic of polarization-driven switching[65], as opposed to filamentary-based switching due to electrochemical migration and/or oxygen vacancy motion (Methods). **e,** *I-V* hysteresis dc sweep ruling out non-polarization-driven resistive switching mechanisms (Methods). The device demonstrates *I-V* hysteresis at low voltage and voltage polarity-independent *I-V* hysteresis-sense; such behavior rules out resistive switching mediated by dielectric breakdown and filamentary mechanisms[64] and is consistent with polarization-driven switching.

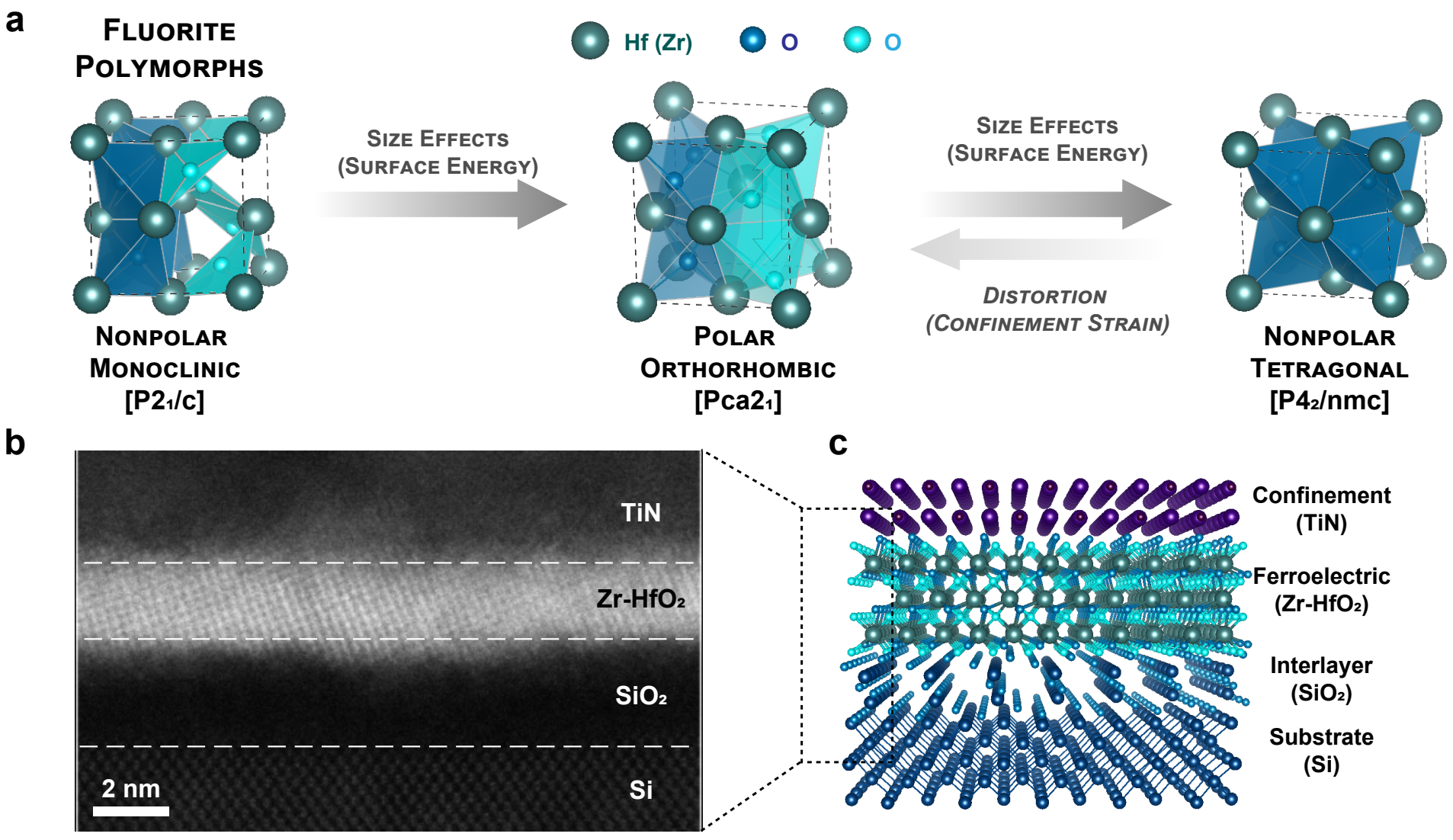
a
Fluorite Polymorphs
Hf (Zr)
O
O
Size Effects (Surface Energy)
Size Effects (Surface Energy)
Distortion (Confinement Strain)
Nonpolar Monoclinic [P2₁/c]
Polar Orthorhombic [Pca2₁]
Nonpolar Tetragonal [P4₂/nmc]
b
TiN
Zr-HfO₂
SiO₂
Si
2 nm
c
Confinement (TiN)
Ferroelectric (Zr-HfO₂)
Interlayer (SiO₂)
Substrate (Si)

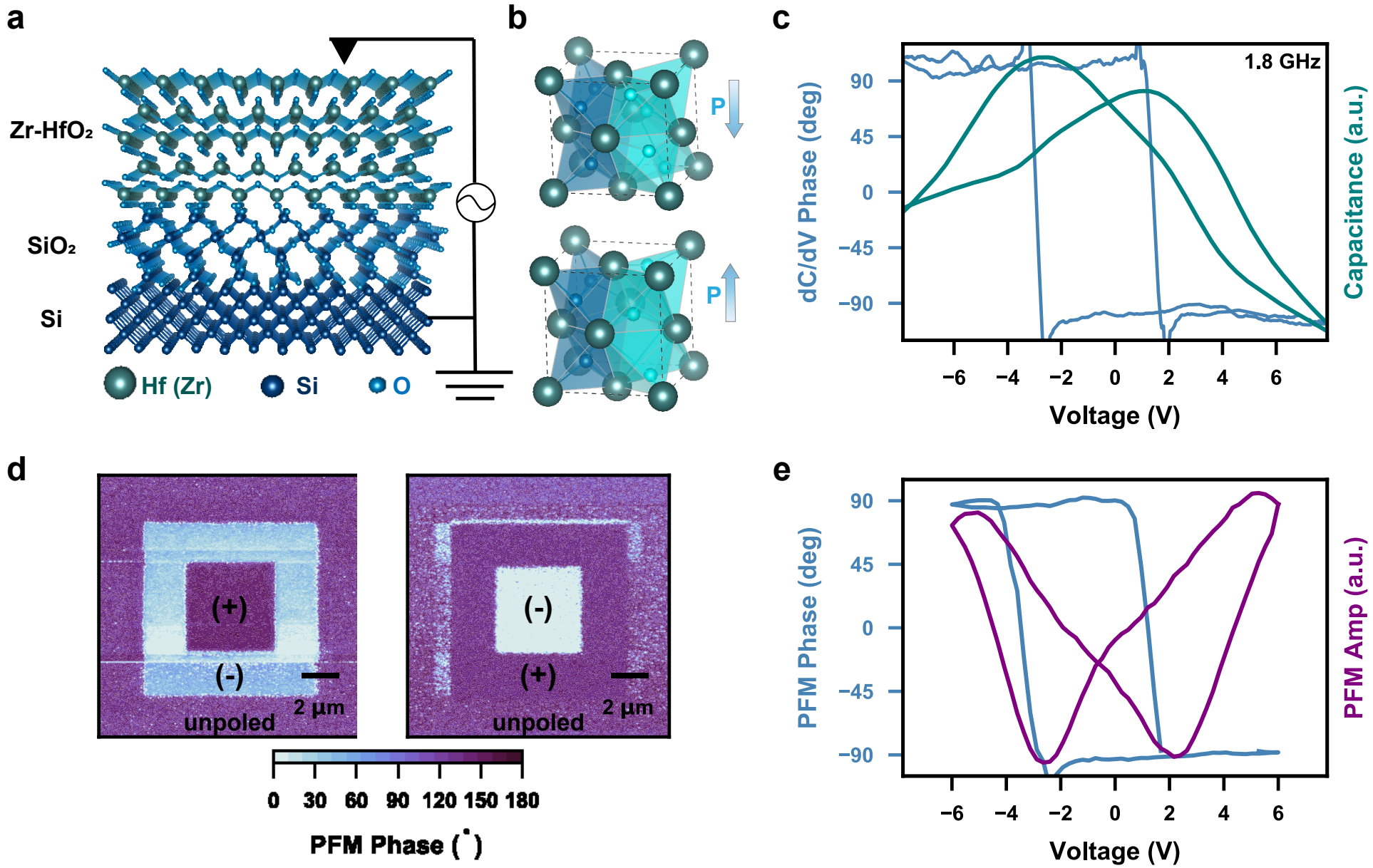
a
Zr-HfO₂
SiO₂
Si
Hf (Zr)
Si
O
b
P
P
c
1.8 GHz
dC/dV Phase (deg)
Capacitance (a.u.)
90
45
0
−45
−90
−6
−4
−2
0
2
4
6
Voltage (V)
d
(+)
(-)
unpoled
2 µm
(-)
(+)
unpoled
2 µm
0
30
60
90
120
150
180
PFM Phase (°)
e
PFM Phase (deg)
PFM Amp (a.u.)
90
45
0
−45
−90
−6
−4
−2
0
2
4
6
Voltage (V)

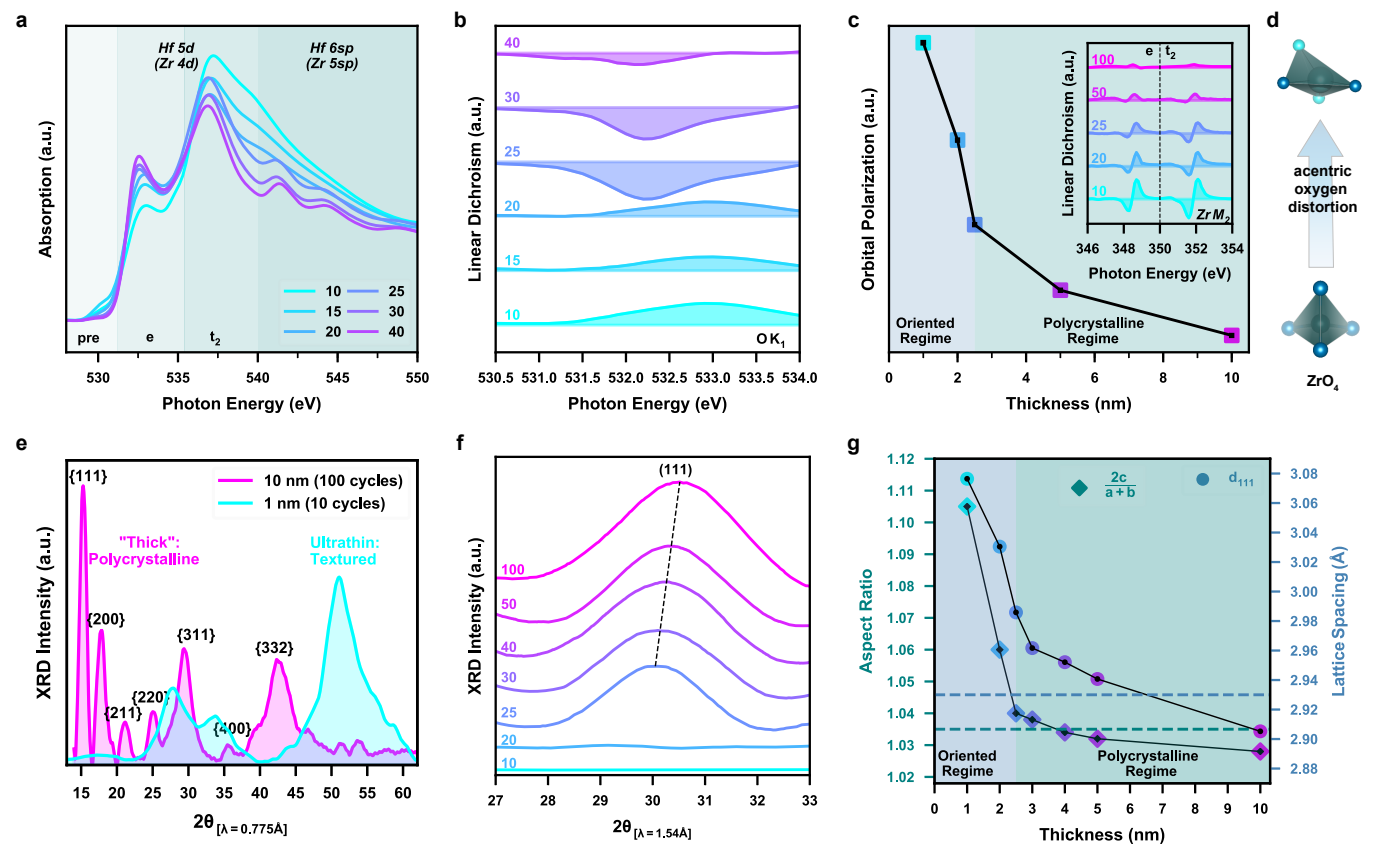
a
Hf 5d
(Zr 4d)
Hf 6sp
(Zr 5sp)
Absorption (a.u.)
pre
e
t2
10
15
20
25
30
40
530
535
540
545
550
Photon Energy (eV)
b
Linear Dichroism (a.u.)
40
30
25
20
15
10
O K1
530.5 531.0 531.5 532.0 532.5 533.0 533.5 534.0
Photon Energy (eV)
c
Orbital Polarization (a.u.)
Oriented
Regime
Polycrystalline
Regime
0 2 4 6 8 10
Thickness (nm)
Linear Dichroism (a.u.)
e
t2
100
50
25
20
10
Zr M2
346 348 350 352 354
Photon Energy (eV)
d
acentric
oxygen
distortion
ZrO4
e
XRD Intensity (a.u.)
10 nm (100 cycles)
1 nm (10 cycles)
"Thick":
Polycrystalline
Ultrathin:
Textured
{111}
{200}
{211}
{220}
{311}
{400}
{332}
15 20 25 30 35 40 45 50 55 60
2θ [λ = 0.775Å]
f
XRD Intensity (a.u.)
(111)
100
50
40
30
25
20
10
27 28 29 30 31 32 33
2θ [λ = 1.54Å]
g
Aspect Ratio
Lattice Spacing (Å)
2c / (a+b)
d111
Oriented
Regime
Polycrystalline
Regime
1.12 1.11 1.10 1.09 1.08 1.07 1.06 1.05 1.04 1.03 1.02
3.08 3.06 3.04 3.02 3.00 2.98 2.96 2.94 2.92 2.90 2.88
0 1 2 3 4 5 6 7 8 9 10
Thickness (nm)